# Long Term Monitoring of Ionospheric Anomalies to Support the Local Area Augmentation System

Jiyun Lee*
*Tetra Tech AMT*
Sungwook Jung and Eugene Bang
*Korea Advanced Institute of Science and Technology**
and
Sam Pullen, and Per Enge
*Stanford University*

**ABSTRACT**

Extremely large ionospheric gradients can pose a potential integrity threat to the users of Local Area Augmentation System (LAAS), and thus the development of an ionospheric anomaly threat model is essential for system design and operation. This paper presents a methodology for long-term ionosphere monitoring which will be used to build an ionosphere threat model, evaluate its validity over the life cycle of system, continuously monitor ionospheric anomalies, and update the threat model when necessary. The procedure automatically processes data collected from external sources and networks and estimates ionospheric gradients at regular intervals. If extremely large gradients hazardous to LAAS users are identified, manual validation is triggered. This paper also investigates a simplified truth processing method to create precise ionospheric delay estimates in near real-time, which is the core of long-term ionosphere monitoring. The performance of the method is examined using data from the 20 November 2003 storm and the 31 October 2003 storm. It demonstrates the effectiveness of simplified truth processing within long-term ionosphere monitoring. From the case studies, the automated procedure successfully identified the two worst ionospheric gradients observed and validated to date.

## 1.0 INTRODUCTION

The Local Area Augmentation System (LAAS) was developed to support aircraft precision approach and landing by providing differential corrections and integrity information to aviation users and by monitoring system outages and failures. Many threats pose potential integrity risk to the system. One of the most challenging anomalies to mitigate is extreme ionospheric spatial gradients that may occur during severe ionospheric storms. Ionosphere spatial gradients in the slant domain (i.e., along the actual path between satellite and receiver) of as large as 413 mm/km over baselines of 40 – 100 km have been observed in the United States during ionospheric storms since April 2000 [1]. The discovery of gradients of this magnitude was a major surprise to the LAAS community, because the residual range error suffered by a LAAS user at the CAT I decision height (DH) can be as large as 8 meters if undetected by the LAAS ground facility (LGF). It required the development of a worst-case ionospheric threat model for LAAS in the Conterminous U.S. (CONUS), the simulation of worst-case ionospheric errors for LAAS users, and the development of additional mitigation strategies [2], [3].

The current ionospheric threat model for CONUS [1] was derived by processing data corrected from networks of Continuously Operating Reference Stations (CORS) and Wide Area Augmentation System (WAAS) reference stations. The threat is modeled as a spatially linear semi-infinite wedge (parameterized by the slope of the ramp and its width) moving with a constant speed as shown in Figure 1. The extreme values of the parameters were determined through a comprehensive search which took several years [1]. This model was used for safety assessment and System Design Approval (SDA) of the Honeywell SLS-4000 LAAS Ground Facility (LGF) by the Federal Aviation Administration (FAA) for use in CONUS. However, even within CONUS, the SLS-4000 threat model has limitations because it is based upon on a small number of severe ionospheric events whose probability cannot be determined due to the lack of sufficient data. In addition, the receiver separations within the CORS network (typically 40 – 100 km) do not reflect the LAAS architecture (shown in Figure 1), given that the distance between the LGF and users at the CAT I decision height (DH) is no more than 5 – 10 km. Because of these limitations, it is not acceptable to rely upon the existing threat model indefinitely. Instead, ionospheric anomalies will be monitored over the life cycle of LAAS, and the threat model will be updated if necessary.

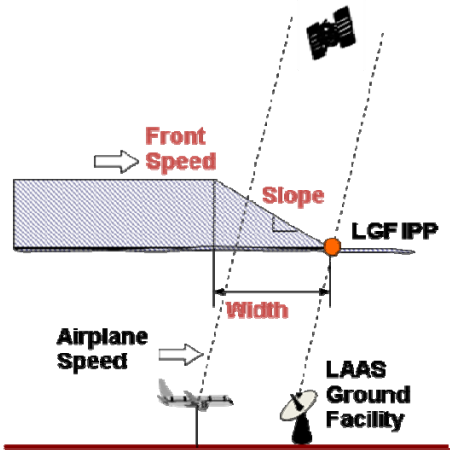


**Figure 1: Illustration of a LAAS user impacted by an ionospheric wave-front (modeled as a linear semi-infinite wedge with the slope of the ramp, its width, and constant propagation speed)**

An automated procedure for long-term ionosphere monitoring is needed to continually monitor ionosphere behavior over the operation period of LAAS as long as LAAS is dependent on the outer bounds of ionospheric threat models. This paper presents a methodology designed to process CORS data (possibly supplemented by data from new stations in future) automatically at regular intervals and to trigger manual data examination if gradients large enough to potentially threaten LAAS users are discovered. Section 2 introduces the dual-frequency GPS data used in this work and briefly describes the extreme ionosphere anomalies which determine the bound of the model. In Section 3, we develop a methodology for long-term ionospheric anomaly monitoring. The effectiveness of the algorithms is examined and the results from case studies are presented in Section 4. This study is concluded in Section 5 with some suggestions on future works.

## 2.0 DATA AND EXTREME IONOSPHERIC GRADIENTS

High-quality ionospheric measurements are required in the development of long-term ionosphere monitoring. The current ionospheric threat model for LAAS was created using precise estimates of ionospheric delays produced by NASA's Jet Propulsion Laboratory. They collected data from the CORS and WAAS network stations and post-processed those in sophisticated algorithms described by Komjathy [4] in order to detect cycle slips, remove integer ambiguities, and estimate the satellite and receiver biases. This JPL solution, so called "Supertruth", is very accurate, but because of time-consuming post-processing algorithms it is not adequate for being used in near real-time applications. Thus, a new method to compute ionospheric delay estimates needs to be developed for this study (the details will be described in Section 3.2.). In this work, we also use dual-frequency GPS data collected from the CORS network [5] to generate precise ionospheric delay estimates.

On 20 November 2003, a coronal mass ejection (CME) from the Sun triggered one of the most severe ionospheric storms of the past solar cycle. This led to a great storm-enhanced density (SED) in the American sector during the local afternoon as shown in the map of vertical ionospheric delays in Figure 2. Dual-frequency GPS slant measurements of the refractive delay of the L1 signal from multiple stations on the ground were converted to their equivalent vertical delays and were plotted on this map. Within this data set, the maximum gradient in slant ionospheric delay as large as 413 mm/km was observed and verified from the previous study [1]. This extreme gradient occurred in between a pair of CORS stations in northern Ohio (ZOB1 and GARF) tracking GPS SVN 38 at high elevation. The most extreme gradient on a low elevation satellite was observed by the WOOS-GARF pair of stations tracking GPS SVN 26, and the magnitude of this slope was about 360 mm/km. These two cases are of particular interest because they determine the upper bound of the slope parameter in the current threat model. We will re-visit those cases in Section 4 to evaluate the performance of the new method proposed for ionospheric delay estimation.

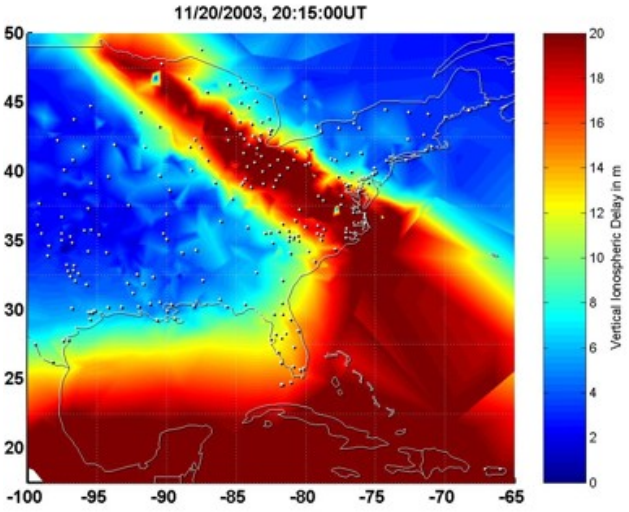


**Figure 2: Map of vertical ionospheric delays over the eastern U.S. on 20 November 2003 20:15 UT**

## 3.0 METHODOLOGY

A detailed methodology for long term ionospheric observation and anomaly monitoring has been developed based on the data-analysis and verification techniques used to generate the current threat model [6]. This procedure is composed of three steps (as shown in Figure 3): External Data Gathering, Internal Processing, and

Manual Validation. The first two steps are completely automated procedures, while the last one is a manual procedure that requires personal intervention. The details of each step are described in the following subsections.

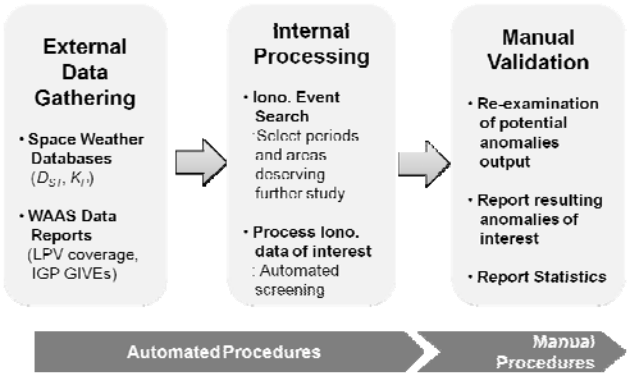


**Figure 3: Methodology of long-term ionospheric anomaly monitoring.**

### *3.1 EXTERNAL DATA GATHERING*

The automated tool first gathers external information from public space weather sites and the WAAS data reports at regular intervals. This external data is used to select potential periods and areas of anomalous ionospheric events in internal processing (which will be described in Subsection 3.2.) In this study, we collect two indices of global geomagnetic activity from space weather databases: planetary K (Kp) and *disturbance, storm time* (Dst). Kp represents solar particle effects on the Earth's magnetic fields, and is a three-hour composite index measured at several mid-latitude stations primarily located in the northern hemisphere [7, 8]. The Kp index ranges from 0 (no activity) to 9 (extreme activity) in thirds of an index unit. The Dst index measures equatorial magnetic disturbance derived from hourly scaling of low-latitude horizontal magnetic variation [9, 10]. A negative Dst with the higher magnitude indicates that the more intense magnetic storm is in progress.

The Kp and Dst indices are available from the ftp server of the National Oceanic and Atmospheric Administration (NOAA) [11, 12]. NOAA provides two types of data for the Kp index: the estimated and final values. The final value provided by the National Geophysical Data Center (NGDC) of NOAA is not adequate for this monitoring system because of a low data rate (updated on a monthly basis 0). Instead we use the estimated value of Kp provided by the Space Weather Prediction Center (SWPC) of NOAA with an update rate of every three hours 0. NGDC also provides three types of Dst: the final, preliminary, and real-time values. However, the latency of data is approximately a month at shortest. An alternative source we choose for the real-time Dst is the World Data Center for Geomagnetism at Kyoto University 0. Their data (known as "Quick-look") are updated every hour.

In order to test the validity of use of the Dst data from Kyoto University, we first compared the final Dst of Kyoto University to that of NGDC and confirmed those are identical. Second, the accuracy of the "Quick-look" data was examined by comparing those with the final values. We also evaluated the validity of the estimated Kp from SWPC as opposed to the use of the final Kp from NGDC. The results showed that the qualities of both the real-time Dst and estimated Kp are good enough to be used in this study.

The WAAS test team of the FAA William J. Hughes Technical Center provides ionospheric vertical delays and Grid Ionospheric Vertical Errors (GIVEs) at geographically fixed Ionospheric Grid Points (IGPs) [14]. They update this information every three minutes. The WAAS GIVEs, contained in WAAS Message Type (MT) 26, can be used an indicator of anomalous ionosphere. Especially in this work, the potential areas where ionospheric anomalies may be discovered are selected based on the GIVEs at each grid point (see Subsection 3.2.)

### *3.2 INTERNAL PROCESSING*

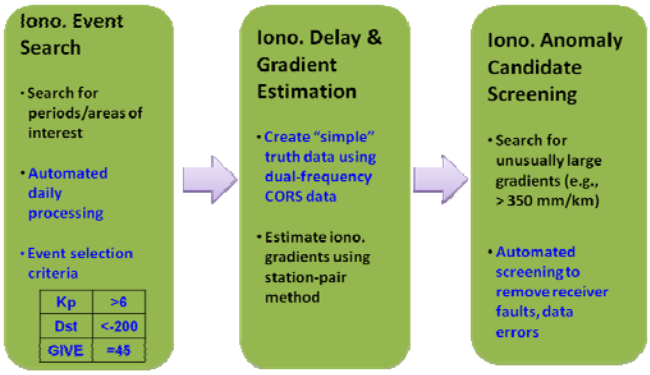


**Figure 4: Procedures of internal processing.**

The second step is internal processing which consists of Ionosphere Event Search (IES), Ionospheric Delay and Gradient Estimation (IDGE), and Ionospheric Anomaly Candidate Screening (IACS). Figure 4 shows the procedures of internal processing. IES selects periods and areas (local clusters of CORS stations) of interest based on the data collected from external sources as explained in Subsection 3.1. IDGE processes data of local clusters and computes ionospheric gradients between stations. This is done by creating "simple Truth" data (meaning simplified but precise ionospheric delay measurements) using dual-frequency CORS data. IACS is designed to automatically search for any anomalous gradients which exceed a threshold and also pass automated false-alarm

screening. The selected anomaly candidates will be manually validated at the last step (the details are in Section 3.3)

*a. Ionosphere Event Search (IES)*

The automated tool processes the external data on a daily basis (as a default) and flags potential periods and areas of severe ionopsheric storm conditions for further automated analysis. First, a particular day is selected if the daily maximum value of Kp is greater than six and that of Dst is less than -200. We pre-determined these selection criteria carefully which satisfy the requirement of discriminating all potential storm periods conservatively while minimizing false detection. If these criteria are applied to the data from 2000 to 2004 which includes the most recent solar maximum period, all dates from which data have been analyzed to build the current CAT I threat model (listed in Table 1) are selected except two dates, 7 Sept. 2002 and 17 July 2004. However, from the fact that no threat points within the threat model have been derived from those two dates, we confirm the selection thresholds are well determined. Second, the daily maximum of GIVE is computed for each IGP and any IGP which has the maximum GIVE value of 45 meters is flagged (the GIVE of 45 meters indicates an abnormal condition by definition). The stations within the grids of selected IGPs are then chosen for further analysis.

**Table 1: Ionospheric storm dates and geomagnetic conditions** Error! Reference source not found..

| Day (UT mm/dd/yy) | $K_p$ | $D_{st}$ | Geomagnetic Storm class |
|---|---|---|---|
| 04/06/00 | 8.3 | -287 | Severe |
| 04/07/00 | 8.7 | -288 | Extreme |
| 07/15/00 | 9.0 | -289 | Extreme |
| 07/16/00 | 7.7 | -301 | Strong |
| 09/07/02 | 7.3 | -163 | Strong |
| 10/29/03 | 9.0 | -345 | Extreme |
| 10/30/03 | 9.0 | -401 | Extreme |
| 10/31/03 | 8.3 | -320 | Severe |
| 11/20/03 | 8.7 | -472 | Extreme |
| 07/17/04 | 6.0 | -80 | Moderate |

*b. Ionospheric Delay and Gradient Estimation (IDGE)*

Once the clusters of CORS stations are selected from IES, the automated tool collects dual-frequency GPS data from the CORS network ftp server. Those data are used to generate precise ionospheric delay estimates. Truth processing removes obvious cycle slips from raw data, "levels" carrier-phase measurements using code measurements, and estimates satellite/receiver inter-frequency biases (IFB). In this section, we explain the method of generating "simple Truth" data, which is simpler and faster than "Supertruth" processing, and the method of estimating ionospheric gradients using the "simple Truth" solutions.

The slant ionospheric delay on the L1 frequency, $I$, is computed from the L1/L2 code ( $\rho_{L1}, \rho_{L2}$ ) and carrier ( $\phi_{L1}, \phi_{L2}$ ) measurements as shown in Equation (1) [15].

$$
\begin{aligned}
I_\rho &= \frac{\rho_{L2} - \rho_{L1}}{\gamma - 1} = I + \frac{c}{\gamma - 1}(IFB_i + \tau_{gd}^k) + \varepsilon_\rho \\
I_\phi &= \frac{\phi_1 - \phi_2}{\gamma - 1} = -I + \frac{c}{\gamma - 1}(IFB_i + \tau_{gd}^k) + \frac{N_{L2} - N_{L1}}{\gamma - 1} + \varepsilon_\phi \\
\gamma &= \frac{f_{L1}^2}{f_{L2}^2}
\end{aligned}
\tag{1}
$$

The ionospheric error $I$ is of equal magnitude but opposite sign on the carrier phase relative to the code phase. The ionospheric delay at the L2 frequency ($f_{L2}$) is proportional to the delay $I$ at the L1 frequency ($f_{L1}$) by the squared frequency ratio $\gamma$. The carrier phase measurements contain integer ambiguities, $N$, on both of the L1 and the L2 signals. The hardware difference in the L1 and L2 signal paths causes inter-frequency biases on both the $i^{th}$ receiver (IFB) and $k^{th}$ satellite ($\tau_{gd}$). The parameter $c$ is the speed of light in a vacuum. The dual-frequency code-derived observable $I_\rho$ is noisier than the carrier-derived observable $I_\phi$ because the carrier phase measurements have lower multipath and thermal noise errors than the code measurements (i.e., $\varepsilon_\phi << \varepsilon_\rho$). Thus, $I_\phi$ is used to obtain precise estimates of ionospheric delays.

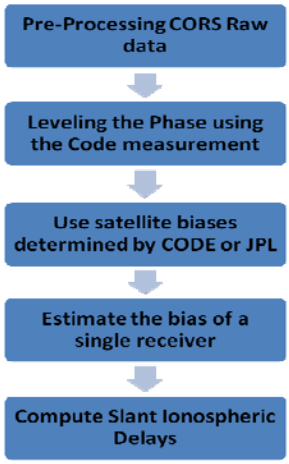


**Figure 5: Algorithm for generating "simple Truth" data.**

Figure 5 shows the procedures of truth processing implemented in the automated tool. The algorithm is as follows. We first perform pre-processing on the code-derived, $I_\rho$ , and carrier-derived, $I_\phi$ , observables, which includes cycle slip detection and correction, short arc removal, outlier removal, and code-carrier smoothing. Cycle slip detection is performed for each continuous arc (which contains data points of more than ten minutes in duration and whose data gaps between adjacent points are less than five minutes.) Three detection criteria are

applied to identify cycle slips of carrier-derived observables. First, a difference between two adjacent data points is examined to detect a large jump (greater than 10 meters). Second, the Loss of Lock Indicator (LLI) of each observation from raw GPS data in RINEX format is utilized as an indicator of potential cycle slips. Third, the absence of both code and carrier measurements is considered as a slip. We discard data arcs less than ten minutes because the leveling error of very short arcs is typically large and thus make delay estimates useless.

After the detection of cycle slips, outlier detection and removal are carried out for each continuous arc. Two approaches, the polynomial fit method and the adjacent point difference method, are executed in parallel. First, a polynomial fit is performed on the carrier-derived observables, $I_\phi$, and the differential residuals of the fit are computed. If the largest jump between adjacent points exceeds an outlier (or slip) detection parameter of 0.8 meters, the jump is classified as a potential outlier. Second, the difference of $I$ between adjacent points is computed using the adjacent point difference algorithm in [16]. The averaged difference (i.e., Outlier Factor (*OF*)), between adjacent points of point $p$ at time $t_p$ is calculated by Equation (2).

$$OF(t_p) = \sum_{q \in Adjacent} w_{pq} \cdot \left| I_p - I_q \right|$$
$$w_{pq} = \frac{1/\left| t_p - t_q \right|}{\sum_{r \in Adjacent} 1/\left| t_p - t_r \right|} \qquad (2)$$

The set "*Adjacent*" includes all points within five minutes centered at the point $p$. $w$ is the weight between two points, $p$ and $q$. This process is repeated until no more outliers remain. As for the last step of pre-processing, we apply a five-minute carrier-smoothing window to smooth the 30-second code-derived observables, $I_\rho$, in order to mitigate multipath errors on the code measurements.

As shown in Equation (1), the carrier-derived observable, $I_\phi$, contains integer ambiguities from both L1 and L2 frequencies. To remove these ambiguities, $I_\phi$ is fitted to $I_\rho$, introducing a level parameter, $L$ [4, 17].

$$L = \frac{\sum_{i=1}^{N} \left( I_\rho(t_i) - I_\phi(t_i) \right) \sin^2 el_i}{\sum_{i=1}^{N} \sin^2 el_i} \qquad (3)$$

The level is computed for each continuous arc by averaging the difference between $I_\rho$ and $I_\phi$ over the epoch $t_i$ using an elevation (*el*)-dependent weighting. Since the code observables at low elevation angle are affected by larger multipath errors, low elevation data are weighted less. To mitigate the multipath effects further, data with elevation angles less than 10 degrees are discarded (only within this leveling step). The leveled carrier-derived estimates, $I_{\phi\_leveled}$, can be written as

$$I_{\phi\_leveled} = I_\phi + L = I + \frac{c}{\gamma - 1}(IFB + \tau_{gd}) \qquad (4)$$

In Equation (4), the receiver and satellite hardware biases (*IFB* and $\tau_{gd}$) must be removed to obtain ionospheric delay estimates, $I$.

The next step is to calibrate inter-frequency biases. We follow Ma and Maruyama [17], in which a simpler and faster method to estimate a single receiver IFB is proposed under the condition that satellite biases are known. The underlying assumption of this method is that the variation of vertical ionospheric delays from all visible satellites at a given instant becomes minimal when the IFBs are correctly removed. The leveled carrier-derived estimates, $I_{\phi\_leveled}$, from Eq. (4) are converted to equivalent vertical delays via a geometric mapping function, and used as inputs to a search algorithm. The best estimate of each receiver IFB is determined by searching for the one which minimizes the cumulative standard deviation of vertical ionospheric delays to their mean on a given day. To improve estimation accuracy in ionospherically abnormal conditions and also to reduce processing time, we searched for the optimal elevation cut-off angle by trying out a wide range of candidates. The resulting cut-off angle applied for this algorithm is 35 degrees.

Last, the automated tool computes ionospheric gradients from all possible pairs of selected CORS stations looking at each satellite. We use the well-known station pair method [1] where pairs of stations in the "simple Truth" solution are considered as though they represent an LGF-user receiver pair. The gradient of ionospheric delay, $\nabla I$, is estimated by dividing the differential slant delay between two stations $i$ and $j$ looking at the same satellite $k$ by the baseline distance between two receivers at each epoch $t$.

$$\nabla I(t) = \frac{\left| I_i^k(t) - I_j^k(t) \right|}{\left\| \mathbf{x}_i - \mathbf{x}_j \right\|} \qquad (5)$$

*c. Ionospheric Anomaly Candidate Screening (IACS)*

In Ionospheric Anomaly Candidate Screening (IACS), an automated process searches for any severe ionospheric gradients, $\nabla I$, which exceeds a threshold (currently 350 mm/km in slant domain). A considerably large amount of these gradients is not due to ionospheric events. Thus, an automated false-alarm screening process is added to

eliminate those caused by any receiver faults or post-processing errors. To improve the performance of false-alarm detection, more techniques are added to the existing automated screening method [1]. Cases for which ionospheric delay estimates from one receiver have negative values or do not vary in time are attributed to a faulty receiver and eliminated. These cases often exhibit a large bias on delay estimates resulting in misleading large gradients. Those false gradients are removed by utilizing the averaged difference (expressed in Equation (2)) of ionospheric gradients. During extreme ionospheric activities, erratic variations of gradients in time are typically observed and an outlier factor computed at the worst gradient point within a continuous arc tends to be large. Thus, gradients which have outlier factors less than 1.6 mm/km are discarded in this process. Another group of false gradients are caused by the poor accuracy of "leveling" (from Equation (3)) especially when data arcs are short. Outlier factors are again computed for these cases, which are eliminated by applying a threshold of 50 mm/km.

### *3.3 MANUAL VALIDATION*

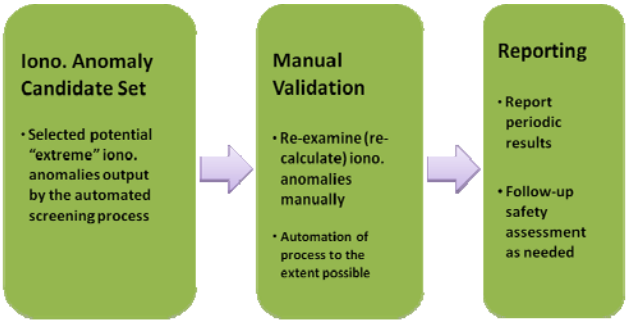


**Figure 6: Procedures of Manual validation and Reporting.**

Once the automated tool has isolated an apparently anomalous set of data, manual inspection is required to validate that the observed events are actually due to the ionosphere and not CORS receiver faults or data errors. While approaches to manual validation will vary based on the details of the automated outputs, the typical method is to re-examine the L1/L2 dual-frequency estimates visually to determine whether the resulting gradients look "reasonably" like ionospheric events. Dual-frequency data are prone to L2 (semi-codeless) loss of lock, particularly for satellites at low elevation angles. Even after detecting cycle slips and removing obvious outliers on dual-frequency measurements, the dual-frequency delay estimates can be corrupted by remaining receiver artifacts. The automated screening to eliminate large gradients caused by post-processing errors is not faultless either. Therefore, we compare the dual-frequency estimates with the estimates based on only the L1 frequency code-carrier divergence. This L1-only measurement is more robust to outages and cycle slips. If both the dual-frequency and single-frequency estimates are in agreement, the gradient is declared to be "validated."

If an anomalous event is substantially validated by manual analysis, it will be reported periodically along with gradient statistics. It is expected that commonly nothing requiring manual validation is found in a given time period. In that case, ionospheric statistics from automated procedures will be supplied in periodic reports. The reports will occasionally be filled with manual validation results in addition to automated results statistics. These results would be reviewed and, if they exceed the bounds of the current threat model, a change to that model would be considered.

## 4.0 RESULTS FROM CASE STUDIES

To examine the performance of the automated algorithms, this section shows example results for long term ionosphere monitoring based upon re-processing the existing ionospheric storm data and comparing the results to those generated previously by offline manual analysis. The first test was conducted on the 20 November 2003 ionospheric storm during which the largest gradients were observed to date. The results of the automated procedures at each step are as follows.

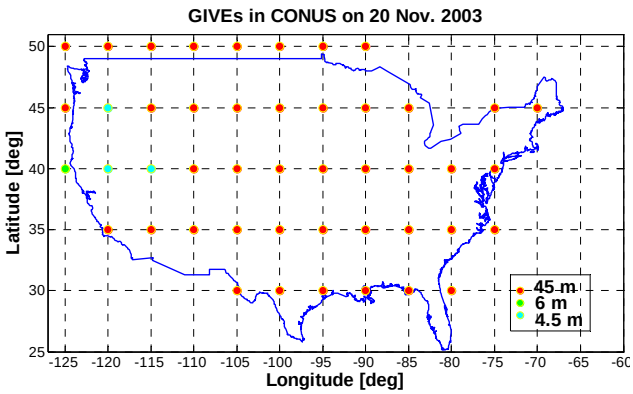


**Figure 7: Daily maximum of WAAS GIVEs at ionospheric grid points in CONUS on 20 November 2003. GIVE of 45 m (red) is a reliable indicator of abnormal condition.**

On 20 November 2003, both of the space weather indices, Kp of 8.7 and Dst of -472, exceed the selection criteria. This date is thus automatically selected at the step of ionospheric event search (IES). The daily maximum GIVEs at each IGP are obtained using the automatically collected WAAS data and shown in Figure 7. Almost all IGPs have the daily maximum values of 45 meters (in red), and thus IES conservatively selects the entire CONUS as the area of interest.

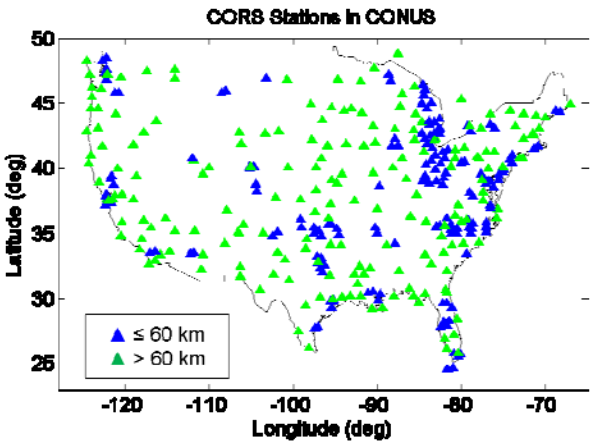


**Figure 8: Map of CORS Stations in CONUS as of November 2003. Those with nearby stations within 60 km are in blue and others are in green.**

Once the area of interest is identified, the clusters of CORS stations for which short baselines can be formed with nearby stations are chosen by applying a selection parameter (60 km was used for this test). The total number of CORS stations within CONUS as of Nov. 2003 is 368 as shown in Figure 8. Among these stations the number of stations which have nearby stations within 60 km (blue) is 173. The GPS dual-frequency data of these stations are automatically downloaded from the CORS ftp server and processed to obtain ionospheric delay and gradient estimates for all pairs of stations considering all satellite in view.

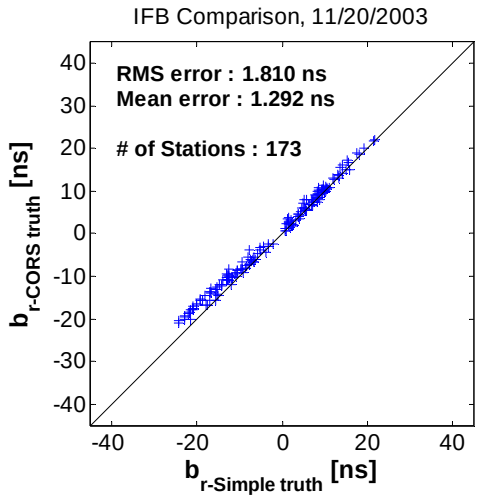


**Figure 9: Comparison of CORS receiver IFB estimates on 20 November 2003. "Simple Truth" receiver biases, $b_{r\_(simple\ truth)}$, are compared to JPL post-processed CORS receiver biases, $b_{r\_(CORS\ truth)}$.**

In IDGE, the raw dual-frequency CORS data are first pre-processed and the carrier-derived ionospheric observables are leveled to the code-derived observables. Next, using the leveled $I_\phi$, the "simple Truth" processing method estimates receiver inter-frequency biases (IFB). In this study, we use satellite biases estimated by the JPL "supertruth" processing in order to directly compare our receiver IFB estimation results to the JPL CORS truth solutions. Figure 9 shows the estimations results of CORS receiver IFB on 20 November 2003. The receiver IFB estimates obtained from the "simple Truth" processing, $b_{r\_(simple\ truth)}$, are compared to the JPL post-processed CORS receiver biases, $b_{r\_(CORS\ truth)}$ generated from the "supertruth" processing. The mean of differences between two solutions is 1.810 ns and the root-mean-square (RMS) error is 1.292 ns. The percentages of the number of stations whose errors are within ±2ns is 72.41. The $b_{r\_(simple\ truth)}$ and $b_{r\_(CORS\ truth)}$ are in a good agreement for a majority of stations, which demonstrates that the "simple Truth" method does a good job of estimating the receiver biases.

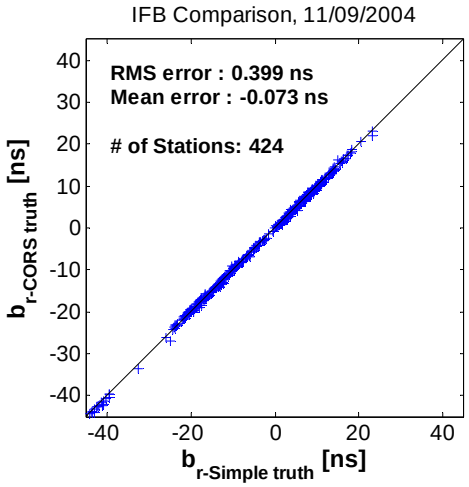


**Figure 10: Comparison of CORS receiver IFB estimates on 9 November 2004. "Simple Truth" receiver biases, $b_{r\_(simple\ truth)}$, are compared to JPL post-processed CORS receiver biases, $b_{r\_(CORS\ truth)}$.**

Figure 10 shows the comparison of CORS receiver IFB estimation results on 9 November 2004. The mean of differences between the "simple Truth" and JPL CORS truth solutions is very close to zero, and the RMS error is 0.399 ns. This statistics are obtained from the total 424 number of CORS receivers, and 99.8 percents of differences are within ±2ns. The underlying assumption of the "simple Truth" method must hold better on ionospherically less active days. Thus, this better performance of bias estimation is expected because the ionosphere activity on this date is less severe than that of 20 November 2003.

After calibrating IFBs, the "simple Truth" solutions, i.e., precise ionospheric delay estimates were generated and the quality of truth solutions was evaluated. Figure 11 shows example results from two stations, ZOB1 and GARF, where the worst gradient at high elevation was

previously discovered. The top plot shows slant ionospheric delays observed between ZOB1 and SVN 38. The "simple Truth" solutions (red) are compared to the WAAS "supertruth" data (green). The lower plot compares two solutions, "simple Truth" (red) and JPL post-processed CORS truth (green) for the slant ionospheric delays on L1 measurements between GARF and SVN 38. For both cases, the two solutions agree well and the discrepancies between two delay estimates are approximately ±1 meter, mainly caused by IFB calibration errors.

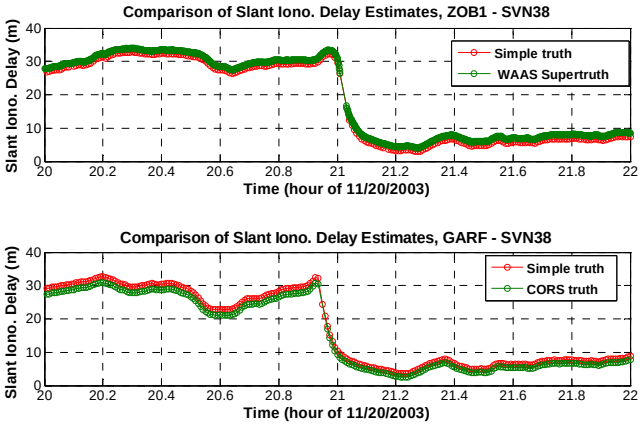


**Figure 11: Comparison of dual-frequency slant ionosphere delay estimates, in meters at L1, for ZOB1 and GARF. "Simple Truth" solutions are in red and "Supertruth" solutions are in green.**

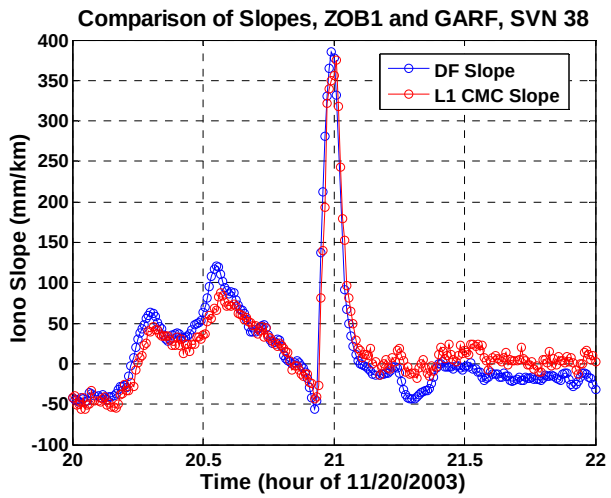


**Figure 12: Comparison of dual-frequency (blue) and single-frequency (red) spatial gradient estimates between ZOB1 and GARF viewing SVN 38 at high elevation, as a function of time.**

Ionospheric gradients were calculated for all possible pairs of 173 CORS stations and all satellite in view. The automated process first searched for any gradients which exceed 350 mm/km for this test, and it returned 35 candidates. Next, automated false-alarm screening process eliminated false candidates caused by receiver faults or post-processing errors, and from that only seven ionospheric anomaly candidates passed this screening. These remaining candidates are of potential concern and thus require manual examination. As expected, the largest gradient at high elevation discovered from the prior work was included in the set of ionospheric anomaly candidates, and further analysis of this case is as follow.

Figure 12 shows the dual-frequency ionospheric gradients (blue) observed from ZOB1 and GARF viewing SVN 38 as a function of time. The gradients are calculated by dividing the difference of the "simple Truth" delay estimates (shown in Figure 11) by the station separation distance of 51.2 km. Data outages on dual-frequency estimates are visible in both Figures 11 and 12, calling into question the reliability of the maximum slope of 385 mm/km at about 68 deg elevation and 2100 UT. For this reason, the manual validation was conducted by comparing the dual-frequency estimates (blue) with the L1 code-minus-carrier estimates of the slope (red). The data outages do not exist in the single-frequency estimates which are not subject to fragile L2 semicodeless tracking loops. Based on the good agreement of the two slope estimates, this event was verified as a real ionospheric anomaly. Note that the magnitude of the slope previously estimated using the JPL post-processed CORS truth data is 413 mm/km. Thus, the discrepancy on gradient estimates between the "simple Truth" and CORS truth is approximately 28 mm/km.

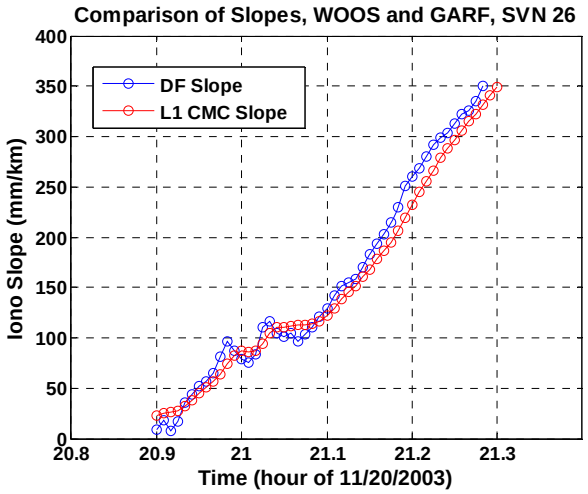


**Figure 13: Comparison of dual-frequency (blue) and single-frequency (red) spatial gradient estimates between WOOS and GARF viewing SVN 26 at low elevation, as a function of time.**

The second trial run of the automated procedures was conducted again on the 20 November 2003 ionospheric storm after adjusting a threshold of CORS station baseline

distances to 80 km. This was done to investigate the largest ionospheric gradient that has been validated at low elevation. Figure 13 compares the dual-frequency-based slope estimates (blue) between WOOS and GARF (which are 75 km apart) viewing SVN 26 with the single-frequency estimates of the slope. Again based on the agreement between two estimates, the highest slope of 350 mm/km occurred at about 12 deg elevation was validated. Since the magnitude of this slope estimated from the JPL CORS truth solution was 360 mm/km, the difference on gradient estimates between two solutions was about 10 mm/km for that case. Despites of the discrepancy, the automated procedures successfully identified the most extreme ionospheric gradients at both high and low elevation, meaning that the "simple Truth" processing is sufficiently accurate.

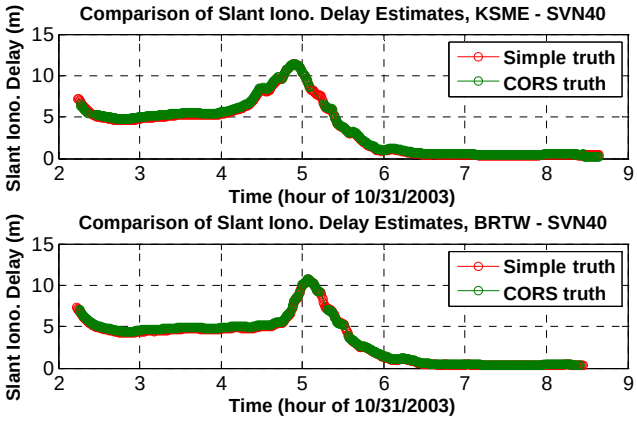


**Figure 14: Comparison of dual-frequency slant ionosphere delay estimates, in meters at L1, for KSME and BRTW. "Simple Truth" solutions are in red and CORS truth solutions are in green.**

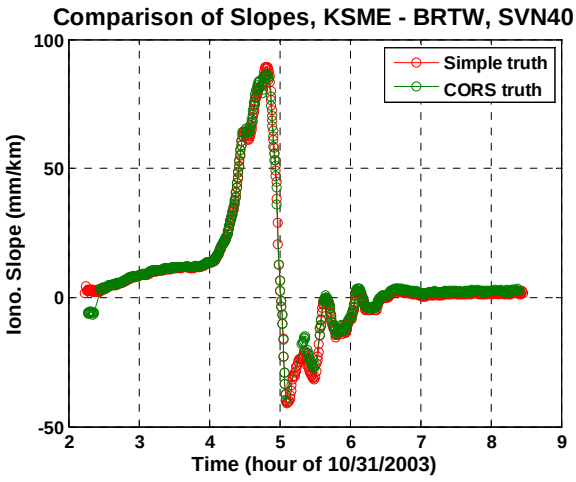


**Figure 15: Comparison of "simple Truth" (red) and CORS truth (green) spatial gradient estimates between KSME and BRTW viewing SVN 40 on 31 October 2003**

The third test was performed on the 31 October 2003 ionospheric storm on which the geomagnetic storm class was "severe" while that on 20 November 2003 was "extreme". Figure 14 compares the "simple Truth" solutions (red) made from two CORS stations, KSME and BRTW, to SVN 40 with the JPL post-processed CORS truth (green) solutions. The two estimates are almost identical because both the leveling error and the receiver IFB estimation error are very small. Note that the "simple Truth" estimates have less data outages that the CORS truth estimates. The slope estimates obtained from two solutions are compared in Figure 15. The "simple Truth" (red) does not contain the apparent cycle slip exhibited in the CORS truth (green) at the early part of the arc. The maximum slope estimated from the "simple Truth" is 89.21 mm/km whereas the result from the CORS truth is 86.39 mm/km. Thus, the difference of gradient estimates is only about 3 mm/km for this example case.

## 5.0 CONCLUSION

This paper presents a methodology of long-term ionosphere monitoring to support the operation of LAAS. The automation of monitoring procedures is necessary to continuously monitor ionospheric behavior by processing the vast amount of CORS data and any additional data from other sources at regular intervals. The validation procedures are also desired to be automated. However, resources for manual validation must be retained because automated results cannot be trusted by themselves. Thus, the automation needs to be improved to further limit the number of "false" gradients passed on to manual validation.

The simplified truth processing is essential to create ionospheric delay estimates without manual intervention. A simpler and faster algorithm to estimate precise ionospheric delays has been described. One variation of this algorithm has been implemented in the long-term ionosphere monitoring tools we developed. The results from case studies support that the quality of "simple Truth" is good enough to identify extreme ionospheric anomalies. However, a request to generate improved (offline) truth data may be needed if they exceed the bounds of the current threat model.

Once these tools are in permanent operation, they will not only observe and quantify extreme ionosphere events but will also supply broader statistical estimates of nominal and anomalous ionospheric behavior. This will help to more accurately categorize nominal and anomalous ionospheric conditions in CONUS. This knowledge should benefit future LAAS operations, including those separate from the "straight-in" CAT I approaches that are now supported. To make this possible, however, more work is needed to improve the reliability and accuracy of "Truth" data.

**ACKNOWLEDGMENTS**

The authors thank the Federal Aviation Administration (FAA) Local Area Augmentation System (LAAS) Program Office, of whom Carlos Rodriguez and Jason Burns were particularly helpful. We also would like to thank Tom McHugh of the FAA William J. Hughes Technical Center for providing the WAAS/NSTB data, Attila Komjathy of the Jet Propulsion Laboratory for processing the dual-frequency CORS/IGS GPS data, Masahito Nose of Kyoto university for providing real-time Dst data, and Ming Luo, Godwin Zhang, Seebany Datta-Barua, Todd Walter, and Juan Blanch of Stanford for their support of this work.

**REFERENCES**

1. Datta-Barua, S., Lee, J., Pullen, S., Luo, M., Ene, A., Qiu, D., Zhang G., and Enge, P., "Ionospheric Threat Parameterization for Local Area GPS-Based Aircraft Landing Systems," AIAA *Journal of Aircraft* , Vol. 47, No. 4, Jul. 2010, pp. 1141-1151.

2. Lee, J., Luo, M., Pullen, S., Park, Y. S., Enge, P., and Brenner, M., "Position-Domain Geometry Screening to Maximize LAAS Availability in the Presence of Ionosphere Anomalies," *Proceedings of ION GNSS 2006*, Fort Worth, TX, Sept. 26-29, 2006, pp. 393 - 408.

3. Ramakrishnan, S., Lee, J., Pullen, S., and Enge, P., "Targeted Ephemeris Decorrelation Parameter Inflation for Improved LAAS Availability during Severe Ionosphere Anomalies," *Proceedings of the 2008 ION National Technical Meeting*, San Diego, CA, Jan. 28-30, 2008, pp. 354 - 366.

4. Komjathy, A., L. Sparks, and A.J. Mannucci, "A New Algorithm for Generating High Precision Ionospheric Ground-Truth Measurements for FAA's Wide Area Augmentation System," Jet Propulsion Laboratory, JPL Supertruth Document, Vol. 1, Pasadena, LA, July 2004.

5. National Geodetic Survey (NGS) CORS Team, "CORS: Continuously Operating Reference Stations," http://www.ngs.noaa.gov/CORS/ [retrieved 12 Aug. 2010].

6. Ene, A., D. Qiu, M. Luo, S. Pullen, and P. Enge, "A Comprehensive Ionosphere Storm Data Analysis Method to Support LAAS Threat Model Development," Proceedings of ION 2005 National Technical Meeting, San Diego, CA., Jan. 24-26, 2005, pp. 110-130.

7. Menvielle, M., and Berthelier, A., "The K-Derived Planetary Indices: Description and Availability," *Reviews of Geophysics*, Vol. 29, No. 3, 1991, pp. 415-432.

8. Menvielle, M., and Berthelier, A., Correction to "The K-Derived Planetary Indices: Description and Availability," *Reviews of Geophysics*, Vol. 30, No. 1, 1992, p. 91.

9. National Geophysical Data Center, "Space Physics Interactive Data Resource," 2005, http:/spidr.ngdc.noaa.gov/spidr/ [retrieved 1 March 2005].

10. Sugiura, M., and Kamei, T., "Equatorial Dst Index 1957–1986," International Association of Geomagnetism and Aeronomy, Vol. 40, 1991, pp. 7–14.

11. National Geophysical Data Center (NGDC) in National Oceanic and Atmospheric Administration (NOAA), "NOAA/National Geophysical Data Center (NGDC) FTP Service," ftp://ftp.ngdc.noaa.gov [retrieved 25 May 2010].

12. Space Weather Prediction Center (SWPC) in National Oceanic and Atmospheric Administration (NOAA), "Space Weather Prediction Center Anonymous FTP Service," ftp://ftp.swpc.noaa.gov [retrieved 25 May 2010].

13. Kyoto University, "World Data Center for Geomagnetism, Kyoto," http://wdc.kugi.kyoto-u.ac.jp [retrieved 28 May 2010].

14. FAA/William J Hughes Technical Center, "NSTB/Wide-Area Augmentation System Test Team" http://www.nstb.tc.faa.gov [retrieved 5 April. 2010].

15. Misra, P., and Enge, P., *Global Positioning System: Signals, Measurement, and Performance,* 2nd ed., Ganga-Jamuna, Lincoln, MA, 2006.

16. Kou, Y., Lu, C.-T., and Chen, D., "Spatial Weighted Outlier Detection," *Proceedings of the 2006 SIAM International Conference on Data Mining*, Bethesda, MD, Apr. 20-22, 2006, pp. 614-618.

17. Ma, G. and Maruyama, T., "Derivation of TEC and Estimation of Instrumental Biases from GEONET in Japan", *Annales Geophysicae*, Vol. 21, 2003, pp. 2083-2093.